2010 American Control Conference
Marriott Waterfront, Baltimore, MD, USA
June 30-July 02, 2010

Design, Characterization, and Control of a Monolithic Three-Axis High-Bandwidth Nanopositioning Stage

Brian J. Kenton and Kam K. Leang†
Mechanical Engineering Department, University of Nevada-Reno
Reno, NV 89557-0312 USA

Abstract— **A new three-axis serial-kinematic nanopositioning stage developed for high-bandwidth applications such as video-rate scanning probe microscopy (SPM) is presented. The stage employs uniquely designed compliant flexures for guiding the motion of the sample platform and to minimize parasitic motion (runout) and off-axis effects compared to previous designs. Finite element analysis (FEA) predicts the dominant resonances along the fast (x-axis) and slow (y-axis) scanning axes at 25.9 and 5.96 kHz, respectively. The performance of the nanopositioning stage is evaluated and the measured dominant resonances in the fast and slow scanning directions are 24.2 and 6.0 kHz, respectively, which are in good agreement with the FEA predictions. The lateral and vertical positioning range of the prototype stage is approximately 9×9 μm^2 and 1 μm, respectively. Experimental atomic force microscope imaging and tracking results for closed- and open-loop feedforward control are presented to demonstrate the performance of the stage.**

I. Introduction

Multiaxis nanopositioning stages are critical in applications such as atomic force microscope (AFM) imaging, fiber optic alignment, and micro- and nano-machining. Particularly, video-rate scanning probe microscopy (SPM) [1] and high-throughput probe-based nanomanufacturing require nanopositioners capable of fast and accurate movements. Control methods such as feedforward- [2] and feedback-based techniques [3] can be employed to improve the operating bandwidth of nanopositioners. On the other hand, *mechanically-stiff* stage designs driven by piezo-stack actuators can provide high-bandwidth positioning in the kHz range. One of the major limitations in positioning speed is low mechanical resonances, and fast operation can be achieved by developing a mechanically-stiff stage.

A wide variety of multiaxis nanopositioning stages have been designed, and Table I summarizes a small collection for comparison. The simplest and effective way to achieve three-axis motion is to employ sectored tube-shaped piezoelectric actuators [4]. However, the mechanical resonance of piezoelectric tube scanners is typically less than 1 kHz in the lateral scan directions, thus limiting the scan speed [5]–[8]. Additionally, the mechanical cross coupling causes undesirable AFM-image distortion [8]. In general, the maximum positioning bandwidth in open-loop without compensation is $1/100^{th}$ to $1/10^{th}$ of the dominant resonance [2]. Shear piezos because of their geometry have very high mechanical resonances [9]. The major drawback of shear-type piezoactuators is they provide limited range, typically less than 1 μm. Tuning forks have been implemented in both sample scanning [10] and in probe scanning SPMs. The tuning-fork-based sample scanners are mechanically simple, but the small dimensions of the quartz tuning fork limits the scan range and the scanning motion is typically sinusoidal. Flexure-guided piezoactuated scanning stages [11], both direct drive serial-kinematic [1], [12] and parallel-kinematic [13] configurations, have been developed for high-speed purposes. The advantages of flexure-guided scanners are high mechanical resonances and low cross-coupling. Multiple piezoactuators per degree-of-freedom (DOF) have been used to increase range and scanning bandwidth, but at the cost of increased power to drive the piezoactuators at high frequencies [1], [13]. Designs which involve mechanical amplification have been studied to increase range without having to increase the actuator's length [11], [14]. However, the added mass of the mechanical amplifier along with the flexible linkages lowers the mechanical resonance. In general, a tradeoff must be made between range and speed.

TABLE I
SHORT SUMMARY OF NANOPOSITIONERS.

Configuration	Range (μm)	Dominant Res. (kHz)	Imaging/line rate (range)
Tube scanner [5]	125 (x/y)	0.71 (x) 0.70 (y)	122 lines/s (13.5×13.5 μm^2)
Tube scanner Dual stage (z) [6]	n/a	6.35 (x/y) 80 (z)	3 lines/s (25 μm)
Tube scanner Dual stage (z) [7]	100 (x/y) 10 (z)	0.68 (x/y) 23 (z)	6.25 lines/s (25×25 μm^2)
Shear piezo [9]	0.3 (x/y) 0.20 (z)	∼64 >100	80 frames/s (128×128 px^2)
Flexure guided [1]	1 (x) 3 (y) 2 (z)	45 360 ("self")	33 frames/s (100×100 px^2)
Tuning fork (x) Flex. guided (y) [10]	<1 (x) 2 (y)	100 40	1000 frames/s (100×100 px^2)
Flexure guided [13]	13 (x/y) 4.3 (z)	>20 33	7810 lines/s (n/a)
Flexure guided [14]	25 (x/y)	2.73	n/a

†Corresponding author; kam@unr.edu; Voice: +1.775.784.7782.

Motivated by previous work [12], the main contribution of this article is a new three-axis, serial-kinematic high-speed nanopositioning stage which offers approximately $9\times9\times1$ μm range of motion and kHz bandwidth. The proposed design employs a novel flexure geometry to increase the out-of-plane stiffness, thus reducing the effects of cross-coupling (from x/y to z). The off-axis flexure stiffness is enhanced by increasing the quantity of flexures n, decreasing the flexure length L, and thickening each flexure's center cross section. Along the vertical axis (z), a novel plate flexure guides the motion of the sample stage to minimize the effects of bending modes. Such modes can significantly limit the vertical positioning speed by causing the sample platform to rock side-to-side. It is pointed out that for scanning-type applications, one lateral axis operates much faster than the other, and thus the serial-kinematic configuration is practical and cost-effective. This configuration has been shown to offer one of the fastest scanning speeds [1], [10]. However, existing serial-kinematic designs offer relatively short range motion, typically less than a few micrometers. The proposed design offers improved operating range compared to previous designs with kHz operating bandwidth.

II. Serial-Kinematic Nanopositioning Stages

Serial-kinematic nanopositioning stages have been proposed for high-speed SPM applications [1], [12]. This configuration is suited for scanning motion, where in the lateral directions one axis moves significantly faster than the other for raster-type scanning. A first-generation serial-kinematic two-axis nanopositioner consisting of multiple parts and assembled using fasteners is shown in Fig. 1 [12]. The high-bandwidth x-axis is nested within the low-speed y-axis. The measured first resonances in the x- and y-axes were 29 kHz and 1.5 kHz, respectively [12]. Piezo-stack actuators were used to move the sample platform and the motion of the platform was guided by stiff compliant flexures to minimize parasitic motion (runout). Since the stage consisted of many parts assembled together to create the complete system, slight misalignment during assembly caused incorrect preload on the flexures and the piezoactuator. And thus, the stage's dynamic response was sensitive to the assembly process and variations in the mounting and boundary conditions.

An improvement to the first-generation design is shown in Fig. 2. For better repeatability, the stage body was manufactured from 7075 aluminum using the wire EDM process to create a monolithic design. Positioning of the sample in the vertical direction is achieved using a piezo-stack actuator embedded into the x-positioning stage. The dominant resonances in the x and y axes were measured at 10 kHz and 2.4 kHz, respectively.

To take advantage of the monolithic design and further increase the mechanical bandwidth, the proposed third-generation design incorporates compliant flexures with improved vertical-stiffness to minimize out-of-plane motion. Also, strategically-placed flexures minimize the sample platform's tendency to rotate (θ_x, θ_y, θ_z) at high frequencies. The stage is designed to ensure that the first resonance in all three axes are axial (piston) modes, rather than off-axis modes which can severely limit scan speed. A functioning prototype is shown in Fig. 3 and the details of the design, characterization, and control are discussed next.

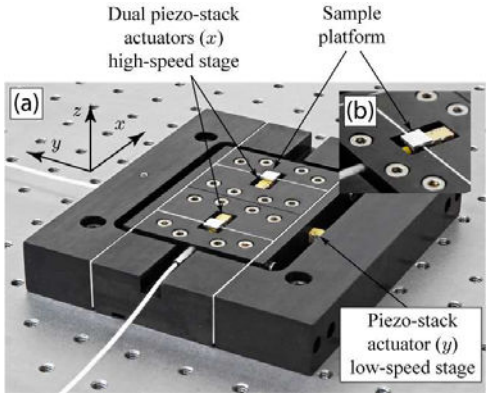

Fig. 1. First-generation two-axis serial-kinematic high-speed scanner, where the high-speed stage (x) is nested inside of the low-speed stage (y). Inset: A close-up view of sample platform and x-axis piezo-stack actuator.

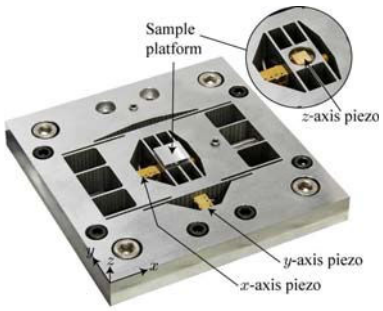

Fig. 2. Second-generation three-axis serial-kinematic stage. The monolithic design was fabricated using wire electric discharge machining.

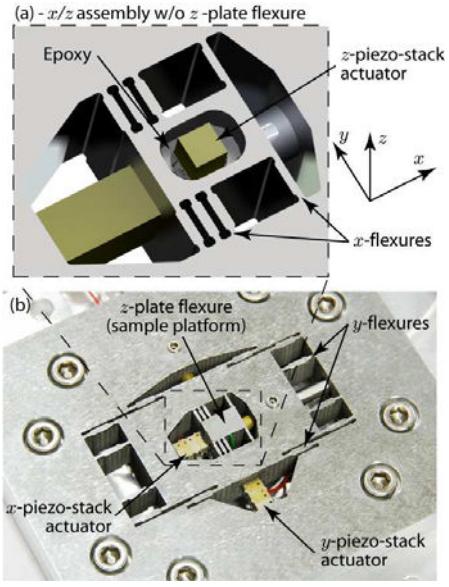

Fig. 3. Third-generation three-axis serial-kinematic nanopositioner: (a) a zoomed-in detailed view of the z piezo-stack actuator assembly with vertically-stiffened x-flexures and (b) the full stage body, x (high-speed) and y (low-speed) axis piezoactuators and vertically-stiffened flexures.

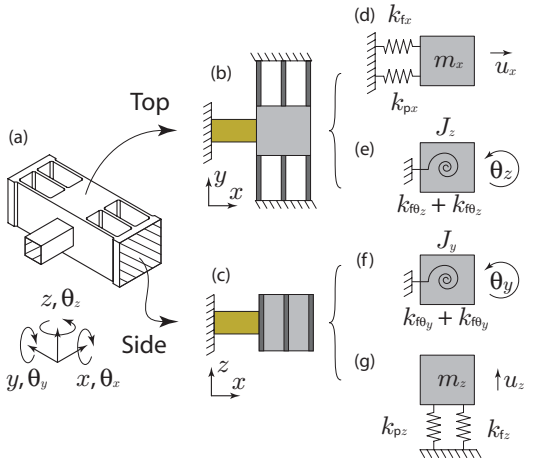

Fig. 4. Generic high-speed stage design simplified to one-DOF systems modeling the dominant resonant modes.

III. Mechanical Design

The use of stiff and compact piezoactuators offers high mechanical resonances, but the cost is reduction in range. The cross-sectional area of the piezo-stack actuators can be increased to improve mechanical stiffness, but doing so will increase the overall capacitance of the piezoactuator, and thus increase the required power to drive the actuator at high frequency. A more practical approach is to focus on improving the design of the flexures which guide the motion of the sample stage. However, one major difficulty is to have the first mechanical resonance occur in the actuation direction. This is particularly challenging since for a relatively long stack piezoactuator, it is much stiffer in actuation compared to bending (for a fixed-free boundary condition). For translational motion u_i ($i = x,\ y,\ z$), the first mechanical resonance is $f_{u_i,0} = \sqrt{k_i/m_i}/2\pi$, where m_i and k_i are the effective translational mass and stiffness, respectively. For rotational motion θ_i ($i = x,\ y,\ z$), the first resonance is $f_{\theta_i,0} = \sqrt{k_{\theta_i}/J_i}/2\pi$, where J_i and k_{θ_i} are the effective mass moment of inertia and rotational stiffness, respectively. Figure 4 shows the simplification of a high-speed x-stage into single DOF systems to model four of the dominating resonance modes. Isometric, top, and side views of the stage are shown in Fig. 4(a) through (c), respectively. The top and side views are broken down into single DOF models showing the effective springs and masses effecting the body for actuation u_x (d), rotational θ_z, (e), rotational θ_y (f), and vertical u_z (g) modes (damping is ignored for convenience). The design objective is to increase the out-of-plane stiffness to mass ratios (k_z/m_z, $k_{\theta y}/J_y$, $k_{\theta z}/J_z$) to be higher than the actuation stiffness to mass ratio k_x/m_x.

A. Flexure Design

The vertical stiffness of the flexures for the x- and y-stages was increased by (1) increasing the number of flexures n, (2) utilizing shorter (effective length) flexures, and (3) converting the flexures from constant rectangular cross section beam flexures to a serial-compliant double-hinged flexure with a "rigid" center connecting link [see Fig. 5(c1)-(c3)]. The latter is referred to as a *thickened* flexure design. The first step taken to increase the flexure stiffness in the vertical direction was studying the affect of how the total number of flexures n used in parallel, flexure thickness t, and length L effect the vertical stiffness k_z for a given actuation stiffness k_i. This comparison was done using both analytical and finite element analysis (FEA).

Consider a generic fix-free cantilever beam flexure shown in Fig. 5(a). The stiffness of a flexure is defined as the ratio of a load F and the resulting displacement u. The displacements and loads are: translational displacement u_i, rotational displacement θ_i, translational force F_i acting on a point in the i direction, and moment M_i (torque T) acting about the i axis (θ_i), where $i = x, y, z$. The in- and out-of-plane compliances for a fixed-free beam are derived using Castigliano's second theorem [15]–[17]. The compliance equations are then used to derive equations for the actuation and vertical stiffness k_i of a fixed-roller guided beam shown in Fig. 5(b1) through (b4). In the second-generation design (Fig. 2) fillet radius is considerably small compared to the flexure length and therefore has minimal impact on the flexure stiffness. For this reason, to simplify the flexure stiffness equations and initial analysis, the compliance equations were derived for a beam with a constant cross sectional thickness.

For a fixed-free beam of rectangular cross section the total strain energy is $U = U_{axial} + U_{torsion} + U_{bending} + U_{shear}$,

$$U = \int_0^L \frac{F^2 ds}{2AE} + \int_0^L \frac{T^2 ds}{2GI_p} + \int_0^L \frac{M^2 ds}{2EI} + \int_0^L \frac{\alpha V^2 ds}{2GA},$$

where L is the beam length, $A = ht$ is the cross sectional area of the beam, h is the height, t is the thickness, E is Young's modulus, $G = E/[2(1+\nu)]$ is the shear modulus, ν is Poisson's ratio, $I_p = ht(h^2+t^2)/12$ is the polar moment of inertia, $I = ht^3/12$ is the second moment of inertia about the vertical z axis, and α is a shape factor for the cross section used in the shear equation (for a rectangular cross section $\alpha = 3/2$) [17], [18]. The displacements u_i and θ_i are found by taking the partial derivatives of U with respect to the applied load, *i.e.*,

$$u_i = \frac{\partial U}{\partial F_i}; \quad \theta_i = \frac{\partial U}{\partial M_i}. \tag{1}$$

From here the compliances are simply found by dividing both sides of the displacement by the applied load, *i.e.*,

$$C_{u_i,F_j} = \frac{u_i}{F_j}; \quad C_{\theta_i,M_j} = \frac{\theta_i}{M_j}. \tag{2}$$

For example, the compliance of the rectangular cross section fixed-free beam in Fig. 5(a) due to a point load in the y direction is found by first finding the total strain energy

$$U = \int_0^L \frac{M(x)^2 dx}{2EI(x)} + \int_0^L \frac{\alpha V(x)^2 ds}{2GA(x)}, \tag{3}$$

where $A(x)$ and $I(x)$ are constants. Substituting in $M(x) =$

$F_y(L-x)$ and $V(x) = F_y$ gives

$$\begin{aligned} U &= \frac{F_y^2}{2EI}\int_0^L L^2 - 2Lx + x^2 d(x) + \frac{\alpha F_y^2}{2GA}\int_0^l d(x) \\ &= \frac{F_y^2 L^2}{6EI} + \frac{\alpha L F^2}{2GA}. \end{aligned} \tag{4}$$

Therefore, the resultant displacement is

$$u_y = \frac{\partial U}{\partial F_y} = \frac{FL^3}{3EI} + \frac{\alpha L F_y}{GA}, \tag{5}$$

and the compliance is

$$C_{yy} = C_{22} = \frac{u_y}{F_y} = \frac{L^3}{3EI} + \frac{\alpha L}{GA}. \tag{6}$$

The compliance equations (or values) are then used to form the multi dimensional compliance matrix $\mathbf{C}$ which is defined as the ratio of the displacement $\mathbf{U} = [x\ y\ \theta_z\ z\ \theta_y]^T$ for a given load $\mathbf{L} = [F_x\ F_y\ M_z\ F_z\ M_y]^T$. This equation is more commonly seen as

$$\begin{Bmatrix} u_x \\ u_y \\ \theta_z \\ u_z \\ \theta_y \end{Bmatrix} = \begin{bmatrix} C_{11} & 0 & 0 & 0 & 0 \\ 0 & C_{22} & C_{23} & 0 & 0 \\ 0 & C_{23} & C_{33} & 0 & 0 \\ 0 & 0 & 0 & C_{44} & C_{45} \\ 0 & 0 & 0 & C_{45} & C_{55} \end{bmatrix} \begin{Bmatrix} F_x \\ F_y \\ M_z \\ F_z \\ M_y \end{Bmatrix}$$

For a constant cross section fixed-free beam the compliance values are $C_{11} = L/AE$, $C_{22} = L^3/3EI + \alpha L/GA$, $C_{23} = L^2/2EI$, $C_{33} = L/EI$, $C_{44} = 4L^3/Eh^3t + \alpha L/GA$, $C_{45} = 6L^2/Eh^3t$, and $C_{55} = 12L/Eh^3t$, where $\alpha = 3/2$. For a long slender beam, shear strain has little effect and can therefore be ignored in C_{22}. For a short beam with a significant height-to-length aspect ratio, such as the vertical displacement of the flexure shown in Fig. 5(b3), much of the deflection is in shear, and therefore can not be ignored. The above matrix equation is used to solve for the actuation stiffness k_y and vertical stiffness k_z of a fixed-guided flexure beam, *i.e.*, $F_i/u_i = k_i$. Figure 5(b4) shows the applied load and the expected deflection curve of the flexure in both the actuation direction (b2) and vertical direction (b3). The active load being applied to the flexure is the in-plane force F_i. The resultant moment $M_i = -1/2F_iL$ is caused by the roller guided end constraint. Therefore, the flexure displacement in the actuation direction u_y due to the applied force F_y and moment $M_z = -1/2F_yL$ is

$$\begin{aligned} u_y &= C_{22}F_y + C_{23}M_z = C_{22}F_y - C_{23}F_yL/2 \\ &= F_y\left[\frac{L^3}{3EI} + \frac{\alpha L}{Ght} - \frac{L}{2}\frac{L^2}{2EI}\right], \end{aligned} \tag{7}$$

where the compliance values C_{ij} are given above. Taking the ratio of the applied load to the displacement, the actuation stiffness (neglecting shear) is

$$k_y = \frac{F_y}{y} = \left[\frac{L^3}{12EI} + \frac{\alpha L}{Ght}\right]^{-1} \cong \frac{12EI}{L^3}. \tag{8}$$

This result matches the fixed-guided Euler-Bernoulli beam equation in [17]. Using the same method, the displacement

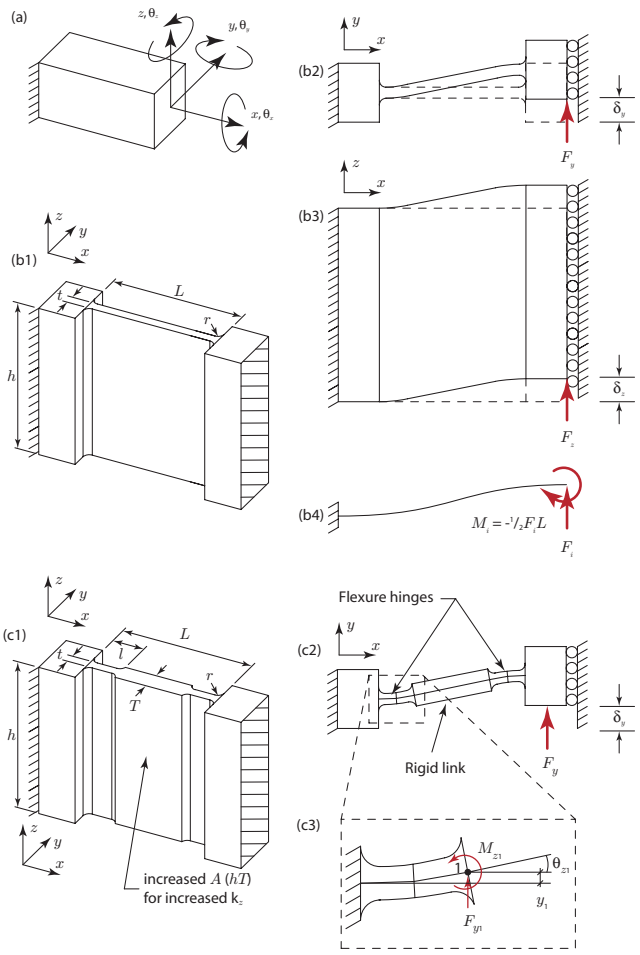

Fig. 5. Flexure design: (a) a fixed-free cantilever beam with six DOFs associated with the applied loads and displacements acting on the free end; (b1)-(b4) is a fixed guided corner filleted beam flexure with corresponding top view, side view, and loads for fixed guided condition, (c1)-(c3) is a fixed guided "thickened" corner filleted beam flexure with corresponding top view and isolated flexure hinge view.

of the flexure in the vertical direction u_z is

$$\begin{aligned} u_z &= C_{44}F_z + C_{45}M_z = C_{44}F_z - C_{45}1/2F_zL \\ &= F_z\left[\frac{4L^3}{Eh^3t} + \frac{\alpha L}{Ght} - \frac{L}{2}\frac{6L^2}{Eh^3t}\right]. \end{aligned} \tag{9}$$

Similarly, the vertical stiffness is

$$k_z = \left[\frac{L^3}{Eh^3t} + \frac{\alpha L}{Ght}\right]^{-1}. \tag{10}$$

Because of the high aspect ratio in the vertical direction, shear can not be ignored.

Equations (8) and (10) are used to study the effect of the quantity of flexures n and flexure thickness t on the effective vertical out of plane stiffness $k_{z\ eff}$. To do this, a given effective actuation stiffness $k_{y\ eff}$ of 10 N/μm was divided by the number of flexures n to give the actuation stiffness for an individual flexure $k_{y\ i}$. Equation (8) is then used to calculate the length L of the individual flexure for a given thickness (0.3 to 1-mm thick). The individual vertical stiffness $k_{z\ i}$ is then calculated using Eq. (10). The individual vertical stiffness is multiplied by the quantity of flexures

to give the effective vertical stiffness. By increasing the number of flexures from 2 to 12 (1-mm thick) the vertical-to-actuation stiffness ratio is increased from 76 to 226 N/μm (197% increase). For $n = 2$, decreasing the flexure thickness from 1 to 0.3-mm thick (which in effect decreases the flexure length) increased the vertical stiffness from 76 to 79.5 N/μm (4.6% increase). Increasing the number of flexures from 2 to 12 and decreasing the flexure thickness from 1 to 0.3-mm thick produces a vertical stiffness of 260 N/μm (242% increase). The red circles in Fig. 6 indicate the $k_{z\ eff}$ values obtained using FEA. The FEA results follow the trend of the analytical results with the only variance being an increase in effective stiffness (average increase = 27%). Increasing flexure height h will also increase vertical stiffness but at the cost of a taller stage body, which increases the mass m and rotational inertia J and reduces the actuation resonance. The most dramatic increase in vertical stiffness for a beam flexure is observed by increasing the number of flexures n. Decreasing the flexure thickness (and as a result the flexure length) increases the vertical stiffness as well. The limiting factor of decreasing the flexure thickness is stress. A shorter thinner beam flexure will have higher stress concentration than a longer thicker beam flexure of equal stiffness.

When a corner filleted beam flexure, as studied above, is displaced in the actuation direction, the majority of the strain is located at the flexure ends near the fillets. Additionally, when the same flexure is displaced in the vertical direction, the majority of the vertical displacement is in shear strain located at the center cross section. An effective way to further increase the out-of-plane stiffness of a beam flexure is to increase the thickness of the center section of the flexure, thus converting the beam flexure into a double-hinged serial flexure as shown in Fig. 5(c1)-(c3). Both analytical and FEA methods were used to study the vertical stiffness of the 'thickened' flexures. The cross-sectional area and second moment of inertia values in Eq. (3) were replaced with $A(x) = ht(x)$ and $I(x) = ht(x)^3$, respectively. For example, the thickness of the flexure in Fig. 5(c1) is

$$t(x) = \begin{cases} t + 2(r - \sqrt{x(2r-x)}) & ,x \in [0,a] \\ t & ,x \in [a,b] \\ t + 2(r - \sqrt{(l-x)(2r-l+x)}) & ,x \in [b,c] \\ t + 2r & ,x \in [c,d] \\ t + 2(r - \sqrt{(l-g)(2r-l+g)}) & ,x \in [d,e] \\ t & ,x \in [e,f] \\ t + 2(r - \sqrt{(g)(2r-g)}) & ,x \in [f,L] \end{cases}$$

where $a = r$, $b = l - r$, $c = l$, $d = L - l$, $e = e + r$, $f = L - r$, $g = L - x$, t and l are thickness and length of the thin section of the flexure, r is the fillet radius, $t + 2r = T$ is the thickness of the thickened section, and L is the length of the entire flexure. For this case, compliance is derived by first solving for the total strain energy [Eq. (3)] while using the thickness function $t(x)$ in the area $A(x)$ and second moment of inertia $I(x)$ equations. For instance, the total strain energy

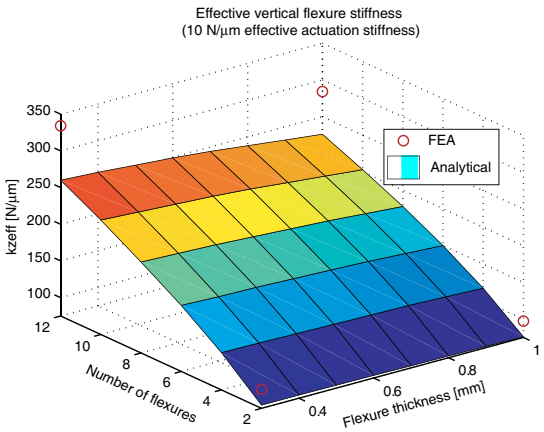

Fig. 6. FEA and numerical analysis results showing effective vertical flexure stiffness $k_{z\ eff}$ with respect to flexure thickness t and quantity of flexures n. Effective actuation stiffness $k_{y\ eff}$ is constant at 10 N/μm.

for bending due to a point load is

$$\begin{aligned} U &= \int_0^l \frac{M(x)^2 dx}{2E\frac{ht(x)^3}{12}} + \int_0^l \frac{\alpha V(x)^2 ds}{2Ght(x)} \\ &= \frac{12F_y^2L^2}{6Eh}\int_0^L \frac{1}{t(x)^3} + \frac{\alpha LF_y^2}{2Gh}\int_0^L \frac{1}{t(x)}. \end{aligned} \quad (11)$$

Taking the partial derivative with respect to the applied force F_y gives

$$u_y = \frac{\partial U}{\partial F_y} = \frac{12F_yL^3}{3Eh}\int_0^L \frac{1}{t(x)^3} + \frac{\alpha LF_y}{Gh}\int_0^L \frac{1}{t(x)}. \quad (12)$$

Table II shows how the vertical stiffness of beam flexures similar to the ones used on the y-stage can be increased an additional 20% by increasing the thickness of the center section. To keep the actuation stiffness $k_{y\ eff}$ constant, the length L of the thickened flexure is increased from 9.75 mm to 10.70 mm.

Flexure placement is important in stage design to increase rotational stiffness. Increasing the length (and width) of a stage and placing flexures at the corners of the moving platform increase rotational stiffness of the platform. The cost of increasing the size of the platform is increased mass and rotational inertia. The highest resonance values are achieved with high stiffness to mass/inertia values.

For the z stage, compliant plate flexures shown in Fig. 3(a) were attached to the ends of the z-piezoactuator shown in Fig. 3(b) to constrain the bending modes. In this case, the piston (along z) mode occurred before the bending mode.

In summary, by increasing the number of flexures n, decreasing the flexure length L, and thickening the center section of a beam flexure to create a serial-compliant double-hinged flexure, the effective vertical stiffness can be improved to increase the out-of-plane stiffness. By adding a plate flexure to the free end of the z-piezoactuator, the first mode shifts from bending to axial (along z axis).

B. Modal Analysis

Modal analysis was done using the *Frequency* and *Linear Dynamic (Harmonic)* FEA tools in COSMOSWorks.

TABLE II

y-AXIS FLEXURE STIFFNESS COMPARISON.

Type	$k_{y\ eff}$ $(N/\mu m)$		$k_{z\ eff}$ $(N/\mu m)$	
	Analytical	**FEA**	**Analytical**	**FEA**
Filleted beam	5.82	6.00	196.6	213.9
Thickened center	5.84	5.32	237.6	238.2

To simplify the analysis, it was assumed that the motion of the nested stages would not excite resonances of the outer stages. The boundary faces of each stage were fixed. All contacting components are bonded to each other with compatible meshing. The meshing was done at "high quality" with refined meshing at the flexure fillets and pivot points. The predicted first mechanical resonance for the y-, x-, and z-stages are 5.96 kHz, 25.9 kHz, and 113 kHz respectively, all in the corresponding stage actuation direction as preferred (see Fig. 7). Simulated frequency response functions with global damping ratio of 0.025 were obtained and compared to the measured responses as shown in Figs. 8(a1) and (b1). The comparison shows good agreement between the predicted and measured results.

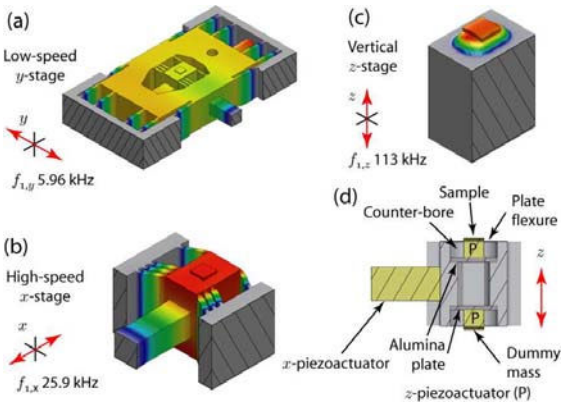

Fig. 7. First mechanical resonance modes for (a) x- (b) y- and (c) z-stages. (d) is a cut-out view of the z stage.

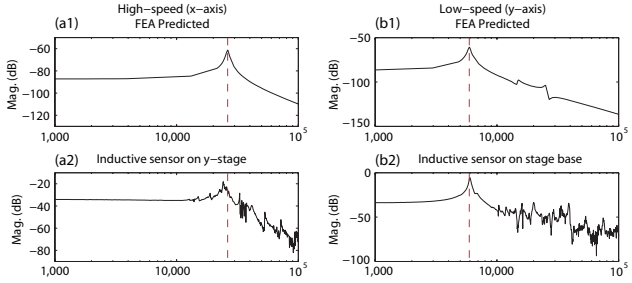

Fig. 8. Predicted and measured frequency responses.

IV. Drive Electronics and Data Acquisition

The drive electronics for the developed stage were designed using off-the-shelf components. The use of off-the-shelf components was preferred to simplify the design and to reduce development time. The fast scanning axes, x and z, require drive electronics capable of supplying sufficient power to drive the capacitive piezoelectric loads at high frequency. The nominal capacitances for the x- and z-axis actuators are

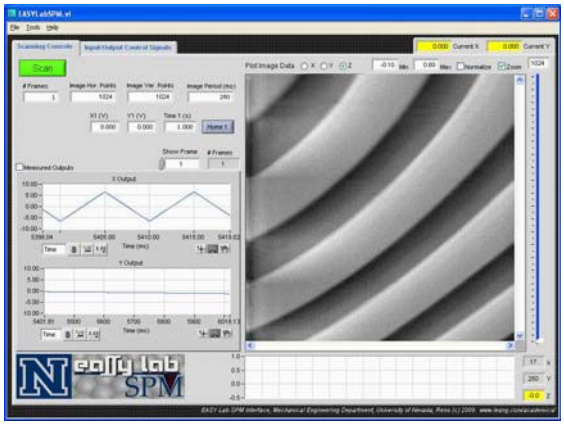

Fig. 9. Custom-designed LabView GUI controlling high-speed data acquisition hardware SPM for imaging (available by contacting the corresponding author).

380 and 50 nF, respectively. The piezo-amplifiers were built around the Power Amp Design (www.poweramp design.net) PAD129 power op-amp, with a gain bandwidth product of 1 MHz. A DC power supply was constructed from two linear regulated 100 V, 3 A DC power supplies (Acopian A100HT300). The two 100 V supplies were wired in series to create a 0 to 200 V supply for the power op-amp. A 33 kHz low-pass filter was cascaded with the power amplifier to reduce the affects of signal stepping from the DAC system used to control piezoactuators.

A LabView SPM control program was created to control the nanopositioning stage for high-speed AFM imaging. The front-end graphical user interface (GUI) is shown in Fig. 9. The program is compatible with National Instrument data acquisition cards that support the NI-DAQmx drivers, for example the NI PCI-6115 high-speed simultaneous sampling data acquisition card, with analog-to-digital conversion bandwidth of 10 MS/s and digital-to-analog output bandwidth of 2.5 MS/s. At this rate, the user can record up to several seconds of 160×160 pixels AFM images with line rates at 8 kHz (50 frames per second).

V. Performance Characterization

The performance of the positioning stage shown in Fig. 3 was experimentally evaluated. The displacements of the sample platform were measured using the Kaman inductive sensor (SMU9000-15N). Application of 180 V peak-to-peak sine input at 100 Hz to the x and y piezoactuators resulted in 7.95 μm and 8.44 μm travel, respectively. Over these ranges, the measured vertical runouts were 27.6 nm peak-to-peak (0.35% or -49.2 dB) caused by actuating the x piezo and 81.4 nm peak-to-peak (0.97% or -40.3 dB) caused by actuating the y piezo. Since the x and y axes can tolerate a maximum of 200 V, the maximum lateral range of the stage is approximately 9×9 μm^2. Frequency response functions were measured using a dynamic signal analyzer (Stanford Research Systems SRT785). Small inputs (<50 mV) were applied to the piezo amplifiers during the test to minimize the effect of nonlinearity such as hysteresis. The measured responses are shown in Fig. 8(a2) and (b2), where the

dominant resonance peak for the x and y axes are 24.2 kHz and 6.0 kHz, respectively. The FEA results are also shown for comparison, with predicted resonances at 25.9 and 5.96 kHz. It is pointed out that the dominant resonances agree with the FEA results, and they are piston (actuation) modes as predicted by FEA.

VI. Controller Design and Results

An analog PID control board was designed to control the positioning along the x and y directions, *i.e.*, to minimize the hysteresis and creep effect in the piezoactuator. Figure 10 shows the block diagram and fabricated board. For the low-speed axis (y), integral control was used with a gain of approximately 30,000. The measured bandwidth of the controller in the y direction was 300 Hz. For the x axis, the PID gains were tuned to $kp = 1.2$, $k_i = 1 \times 10^5$, and $k_d = 1 \times 10^{-5}$. The control bandwidth was 2.5 kHz. For relatively low-speed positioning, integral and PID control were adequate. However, as the scanning speed increases, significant tracking error exists due to dynamic effects. To improve the tracking precision for scanning applications, repetitive control (RC) was added to the PID controller for x-axis positioning. The block diagram of the plug-in RC is shown in Fig. 11, where a signal generator with period T_p is created by a positive feedback loop and pure delay z^{-N}. The positive integer $N = T_p/T_s \in \mathbb{N}$ is the number of points per period of the reference trajectory $r(t)$ and T_s is the sampling period. The plant (*i.e.*, piezoactuator) is assumed to be linear and represented by $G(z)$, where $z = e^{j\omega T_s}$, $\omega \in (0, \pi/T_s)$. The PID controller is represented by $G_c(z)$. The low-pass filter $Q(z)$ in the RC block provides robustness by reducing the effects of high gain at high frequencies. The cut-off frequency of the low pass filter was set to 7 kHz. The parameters for the RC include the RC gain k_{rc} and two phase lead compensators $P_1(z) = z^{m_1}$ and $P_2(z) = z^{m_2}$, where m_1 and m_2 provide a linear phase lead (in units of radians) of $\theta_{1,2}(\omega) = m_{1,2}T_s\omega$, for $\omega \in (0, \pi/T_s)$. The two phase lead compensators can be adjusted to compensate for the phase lag in the closed-loop system and to improve the tracking performance. For the RC system shown in Fig. 11, stability is achieved by ensuring that [19]

$$0 < k_{rc} < \frac{2\cos[\theta_T(\omega) + \theta_2(\omega)]}{A(\omega)} \tag{13}$$

and $|[\theta_T(\omega)+\theta_2(\omega)]| < \pi/2$, where $A(\omega) > 0$ and $\theta_T(\omega)$ are the magnitude and phase, respectively, of the complimentary sensitive function, *i.e.*, $T(e^{j\omega T_s}) = G_0(z)/[1 + G_0(z)] = A(\omega)e^{j\omega T_s}$. The RC was implemented using FPGA hardware, National Instruments cRIO-9002, using $N = 100$, $m_1 = 6$, $m_2 = 0$, and closed-loop sampling frequency of 100 kHz. The RC gain was chosen as $k_{rc} = 0.95$ to satisfy the stability conditions given in Eq. (13). Additional details of RC design for SPM can be found in [19].

The closed-loop tracking results for the x-axis are shown in Fig. 12 comparing PID control and RC for scanning at 1 and 2 kHz. Under PID control, the maximum tracking error are 23.3% and 43.5% at 1 kHz and 2 kHz, respectively. By applying RC, the tracking error was reduced significantly to 4.1% and 6.5%.

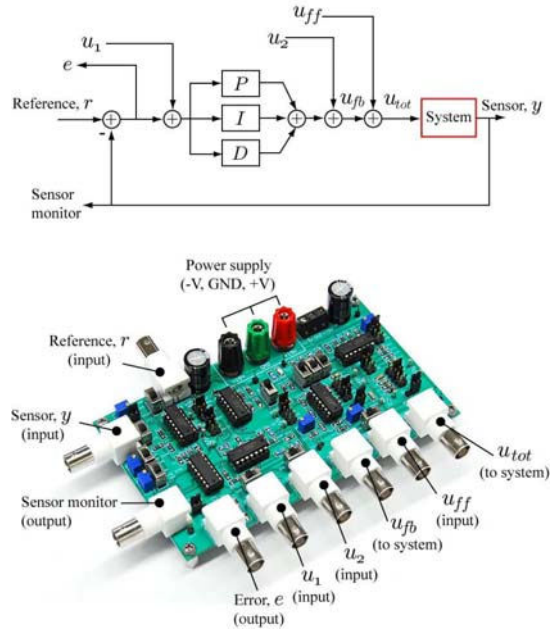

Fig. 10. Custom-designed analog PID feedback controller board.

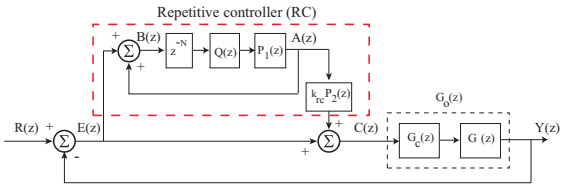

Fig. 11. A plug-in RC with phase lead compensators, $P_1(z)$ and $P_2(z)$, to enhance performance.

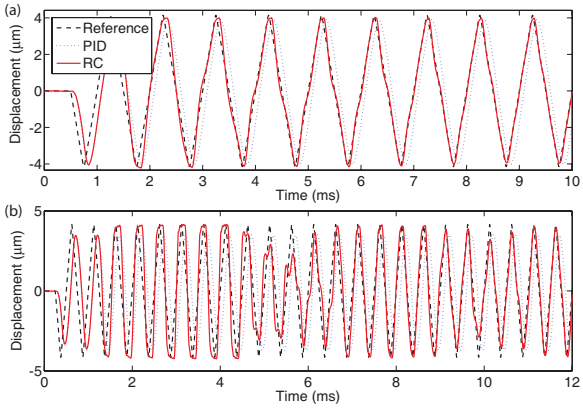

Fig. 12. Tracking results comparing PID and RC: (a) 1 kHz scanning and (b) 2 kHz scanning for x-axis.

To demonstrate the application of the positioning stage, AFM images of a calibration sample (with 3 μm pitch and 20 nm height features) are shown in Fig. 13 up to a line rate of 4 kHz. A NanoSurf easyScan 2 AFM was mounted to the top of the three-axis stage and used to position the AFM probe tip above the sample. A relatively-stiff AFM cantilever with a resonance of 335 kHz was used for contact-mode imaging. The gains for the vertical PI controller were

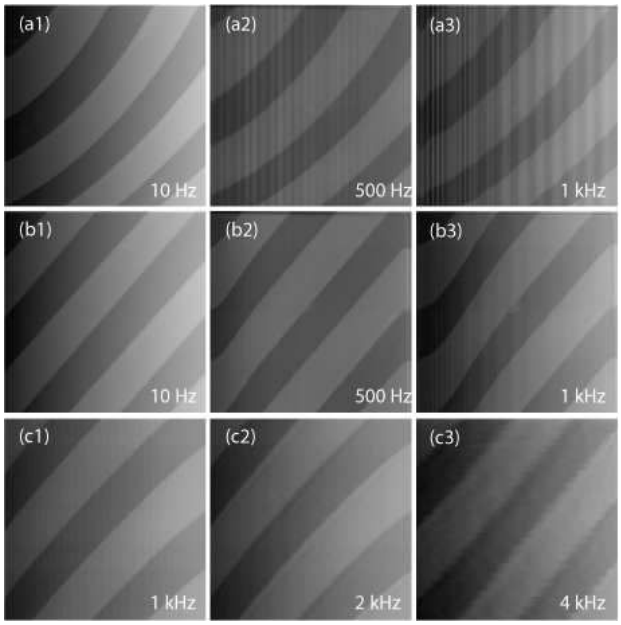

Fig. 13. AFM imaging of a calibration sample with 3 μm pitch and 20 nm height features: (a1)-(a2) open-loop, (b1)-(b3) closed-loop, and (c1)-(c3) phase-compensated sine-wave feedforward.

tuned to compensate for sample tilt during imaging (*i.e.*, $k_p \in [10, 1000]$ and $k_i \in [100, 10, 000]$), yet enable the cantilever to deflect in response to changes in surface features. From the images, it is evident by the appearance of the curved features and vertical bands that the effects of hysteresis, creep, and dynamics in the piezo-stacks are significant in the open-loop uncompensated images (a1)-(a3). Under closed-loop control (PID), the distortion due to hysteresis and the vibration effects are minimized as shown in (b1)-(b3). However, distortions appears along the left and right edge of the image due to the phase shift between the desired and actual response at 500 and 1000 Hz line rate. For high-speed imaging, to avoid exciting the high-order dynamics, a phase-compensated sine wave feedforward input was applied [2]. The line rate can be improved significantly, see (c1) to (c3), up to 4 kHz. Compared to the capabilities of the commercial AFM (scan rate limit is under 10 Hz), the newly developed stage can image with negligible distortion due to dynamics at line rates in the kHz range. In summary, the developed nanopositioning stage offers relatively large range of motion and high-bandwidth positioning for applications that include high-throughput SPM imaging.

VII. Conclusions

A three-axis serial-kinematic nanopositioning stage was developed with mechanical resonances in the kHz range for high-speed applications. Double-hinged serial-flexures were used to guide the motion of the x and y stages and to enhance the stiffness in the out-of-plane direction, thus minimizing the effects of out-of-plane modes. The measured and predicted dynamic responses were in good agreement, and preliminary AFM images acquired at line rates up to 4 kHz were presented. Future work focuses on combined dynamic and hysteresis compensation as well as dual-stage vertical feedback for precision high-speed positioning.

VIII. Acknowledgements

This work is supported, in part, by the Nevada NASA Space Grant Consortium. Authors also thank Pat Leang for his insights and help with developing the LabView GUI front-end for AFM imaging.

References

[1] T. Ando, T. Uchihashi, and T. Fukuma, "High-speed atomic force microscopy for nano-visualization of dynamic biomolecular processes," *Progress in Surface Science*, vol. 83, no. 7-9, pp. 337–437, 2008.

[2] G. M. Clayton, S. Tien, K. K. Leang, Q. Zou, and S. Devasia, "A review of feedforward control approaches in nanopositioning for high speed SPM," *ASME J. Dyn. Syst. Meas. and Cont., Special issue on Dynamic Modeling, Control, and Manipulation at the Nanoscale*, vol. 131, p. 061101 (19 pages), 2009.

[3] B. Bhikkaji, M. Ratnam, A. J. Fleming, and S. O. R. Moheimani, "High-performance control of piezoelectric tube scanners," *IEEE Transactions on Control Systems Technology*, vol. 15, no. 5, pp. 853–866, 2007.

[4] G. Binnig and D. P. E. Smith, "Single-tube three-dimensional scanner for scanning tunneling microscopy," *Review of Scientific Instruments*, vol. 57, no. 8, pp. 1688–1689, 1986.

[5] G. Schitter and A. Stemmer, "Identification and open-loop tracking control of a piezoelectric tube scanner for high-speed scanning-probe microscopy," *Control Systems Technology, IEEE Transactions on*, vol. 12, no. 3, pp. 449–454, 2004.

[6] G. Schitter, W. F. Rijke, and N. Phan, "Dual actuation for high-bandwidth nanopositioning," in *Proc. IEEE Conference on Decision and Control*, Cancun, Mexico, 2008, pp. 5176–5181.

[7] A. J. Fleming, "High-speed vertical positioning for contact-mode atomic force microscopy," in *Proc. IEEE/ASME International Conference on Advanced Intelligent Mechatronics*, Singapore, 2009, pp. 522–527.

[8] O. M. E. Rifai and K. Youcef-Toumi, "Coupling in piezoelectric tube scanners used in scanning probe microscopes," in *American Control Conference*, vol. 4, 2001, pp. 3251 – 3255.

[9] M. J. Rost, L. Crama, P. Schakel, E. van Tol, G. B. E. M. van Velzen-Williams, C. F. Overgauw, H. ter Horst, H. Dekker, B. Okhuijsen, M. Seynen, A. Vijftigschild, P. Han, A. J. Katan, K. Schoots, R. Schumm, W. van Loo, T. H. Oosterkamp, and J. W. M. Frenken, "Scanning probe microscopes go video rate and beyond," *Review of Scientific Instruments*, vol. 76, no. 5, p. 053710, 2005.

[10] L. M. Picco, L. Bozec, A. Ulcinas, D. J. Engledew, M. Antognozzi, M. A. Horton, and M. J. Miles, "Breaking the speed limit with atomic force microscopy," *Nanotechnology*, no. 4, p. 044030, 2007.

[11] F. E. Scire and E. C. Teague, "Piezodriven 50-μm range stage with subnanometer resolution," *Review of Scientific Instruments*, vol. 49, no. 12, pp. 1735–1740, 1978.

[12] K. K. Leang and A. J. Fleming, "High-speed serial-kinematic AFM scanner: design and drive considerations," *Asian Journal of Control, special issue on Advanced Control Methods for Scanning Probe Microscopy*, vol. 11, no. 2, pp. 144–153, 2009.

[13] G. Schitter, P. J. Thurner, and P. K. Hansma, "Design and input-shaping control of a novel scanner for high-speed atomic force microscopy," *Mechatronics*, vol. 18, no. 5-6, pp. 282–288, 2008.

[14] Y. K. Yong, S. S. Aphale, and S. O. R. Moheimani, "Design, identification, and control of a flexure-based xy stage for fast nanoscale positioning," *Nanotechnology, IEEE Transactions on*, vol. 8, no. 1, pp. 46–54, 2009.

[15] S. P. Timoshenko, *History of Strength of Materials*. New York: McGraw-Hill Book Company, 1953.

[16] N. Lobontiu and E. Garcia, "Two-axis flexure hinges with axially-collocated and symmetric notches," *Computers & Structures*, vol. 81, no. 13, pp. 1329–1341, 2003.

[17] R. R. J. Craig, *Mechanics of Materials, 2nd ed.* New York: John Wiley & Sons, 2000.

[18] W. C. Young and R. G. Budynas, *Roark's Formulas fo Stress and Strain*, 7th ed. New York: McGraw-Hill, 2002.

[19] U. Aridogan, Y. Shan, and K. K. Leang, "Design and analysis of discrete-time repetitive control for scanning probe microscopes," *ASME J. Dyn. Syst. Meas. and Cont., Special issue on Dynamic Modeling, Control, and Manipulation at the Nanoscale*, vol. 131, p. 061103 (12 pages), 2009.